

Development of backgammon-type multiwire proportional counters for the detection of x rays

J. A. Kimpton,^{a)} M. N. Kinnane, and C. T. Chantler

School of Physics, University of Melbourne, Parkville, Victoria 3010, Australia

(Received 16 March 2006; accepted 2 July 2006; published online 2 August 2006)

A multiwire proportional counter (MWPC) based on a backgammon-type design has been developed for the detection of x-ray photons in two dimensions over the energy range of 4–6 keV. The MWPC was designed for operation in an experimental spectroscopy application requiring single photon counting over a wide range of count rates, high photon detection efficiency and resolution, and a highly linear response function across the detector face. A model based on attenuation of the incident x-ray beam by the various components of the detector is presented and highlights key areas for efficiency optimization. The design, construction, testing procedure, and performance of the backgammon MWPC are presented and all objectives are met including a particularly impressive differential nonlinearity. © 2006 American Institute of Physics.

[DOI: [10.1063/1.2237760](https://doi.org/10.1063/1.2237760)]

I. INTRODUCTION

The development of instrumentation to measure the intensity, energy, trajectory, or position of x rays and high energy particles has been a major area of investigation within experimental physics over many decades. The ability of the gas proportional counter to record incident particle or x-ray photon intensity with only a very small amount of primary charge is a unique feature of the detector. The development of the multiwire gas proportional counter (MWPC) has enabled the detection of high energy particles and x-ray photons in multiple dimensions and has introduced further flexibility to the proportional counter.^{1,2} The advancement in charge coupled devices (CCDs) has resulted in multi-dimensional representation of incident x-ray photons with improved resolution. However, two distinct disadvantages of CCD cameras are the inability for single photon counting over a wide range of count rates and the relatively poor real-time energy discrimination (such as cosmic ray filtering). Furthermore, the proportional counter can function over a much larger energy range with simple adjustments to basic parameters (i.e., gas composition, gas pressure, configuration).

The research team at the University of Melbourne has developed a backgammon-type MWPC. This is part of a continuing development of a state-of-the-art Johann curved crystal spectrometer. Our particular key application is to perform critical testing of bound state Quantum Electrodynamics (QED) by measurement of the Lamb shift in medium-*Z* highly charged ions.³ The highly charged medium-*Z* ions are generated in an electron beam ion trap⁴ (EBIT) where the intensity of the x rays generated is relatively low (<1 Hz), therefore a detector designed for this application should possess high photon detection efficiency. A status report on this earlier spectrometry has been presented.⁵ One of the key

needs for transverse imaging in this context relates to off-axis curvature and the calibration of this as a signature of the curved crystal and instrumental systematics.⁶ The energy range of these measurements is relatively small (4–6 keV), but the MWPC is capable of efficient operation over a much larger range (3–9 keV) with minor adjustment, and with further modifications much higher energies can be detected efficiently. An attenuation model for all MWPCs is presented and highlights areas for potential photon detection efficiency improvement.

One of the biggest problems of most imaging detectors is their differential nonlinearity. It is this aspect which destroys the ability of several detector types to determine small (1 μm or 10 μm) shifts of position which must be measured to obtain new unprecedented levels of accuracy in high-precision experiments. Note that the resolution is much less important in this context. Good resolution and a high degree of linear response over the detection area are desirable as the characteristic spectral lines of interest are separated by only a few eV. The detector should also be capable of recording single photon events at high count rates (1–30 kHz) in order for calibration spectra (comprised of characteristic spectral lines in the chosen energy range and generated in an external x-ray source) to be collected more efficiently. The backgammon MWPC, signal processing electronics, and data acquisition system presented is capable of single photon counting for both low and high count rate applications and is described in detail. The signal processing employed is a significant departure from the typical delay line and timing electronics commonly employed for these measurements and simplifies detector construction.

This article covers details of design and construction, signal generation, electronics and data acquisition, testing procedure, and results and discussion. One of the most significant developments is in the area of differential nonlinearity, as detailed below.

^{a)}Electronic mail: jkimpton@unimelb.edu.au

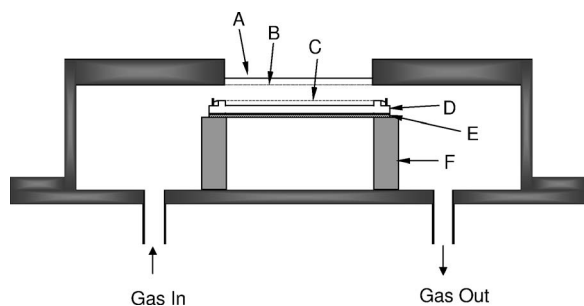


FIG. 1. Cross section of the internal components of the backgammon-type MWPC showing (A) beryllium window, (B) nickel mesh ground plane, (C) platinum anode wire plane, (D) Macor anode wire support, (E) cathode board, and (F) Macor support structure. The region between A and B is the dead zone and should be as small as possible.

II. DESIGN AND CONSTRUCTION

The backgammon MWPC developed in this study follows the work presented by Allemand and Thomas,⁷ Duval *et al.*⁸ and Luther *et al.*⁹ Nonetheless there has been active development in a number of significant areas which have not been presented before. The electronics and processing are quite different. The detector size is much larger, the format and construction are different, and our nonlinearity is far superior and a key new result. The ideas of Ref. 8 and the NIST group (Deslattes *et al.*) led to the development of tools mentioned in Ref. 3. That paper³ used the old-style detector type, with hybrid electronics, but no advanced data processing, to achieve the remarkable results presented therein. As seen below, the differential nonlinearity is dramatically improved as a consequence of these technical developments and allows far superior results to be obtained, subject to simple statistical considerations.

The detector (shown in Fig. 1) consists of four basic components: the ionizing gas, anode wire, cathode board, and grounding plane. Since the electrostatic model for the detector is based on coaxial cylindrical geometry, the anode wire is suspended exactly half way between the grounding plane and the cathode board. The entire assembly is enclosed in a stainless steel body with incident x-ray photons entering through a circular 250 μm thick beryllium window. The diameter and area of the window are 33 mm and 855 mm², respectively. The detection area is more than 32% larger than the model reported by Luther *et al.*⁹ The interior of the detector is filled with an argon (90%) and methane (10%) gas mixture (P10) and sealed with Viton O-rings at the entrance window and rear. The gas pressure is measured with a Baratron-type 722A absolute capacitance manometer. The uncertainty in the pressure measurement is no greater than 1%. Electrical feedthrough and gas ports are located on the rear of the detector.

A 12.7 μm thick electroformed nickel mesh having 70 lines per inch (LPI) forms the grounding plane closest to the beryllium entrance window. The x-ray transmission through this material increases from 86% to 90% for 4 to 6 keV x-ray photons, respectively. To maximize efficiency, the *dead zone* (the region between the beryllium window and the nickel mesh) is minimized, as this volume does not form part of the active detection region. The second grounding plane,

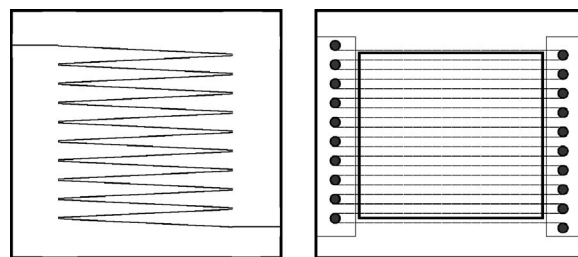


FIG. 2. Cathode board layout (left) showing the two halves of the inter-leaved sawtooth sections separated by a 100 μm wide channel. The anode assembly (right) showing the gold-coated pins mounted in the Macor frame. The anode wire is wrapped in serpentine fashion around each pin forming 19 segments.

or cathode, closely resembles a backgammon board and consists of two gold-coated, interleaved, sawtooth pattern sections separated by a 100 μm wide channel (Fig. 2). The cathode board is constructed from printed circuit board material and each sawtooth section is 40 mm long and 4 mm wide at the base. The points on the cathode segments are truncated in order to reduce nonlinear effects at the extreme edges.^{8,10} The cathode board and nickel mesh are connected to electrical common ground and are the destination for the positive ions generated in the ionization process.

The anode wire consists of a continuous 6.5 μm diameter platinum wire wound around gold-coated pins (2 mm in diameter) in serpentine fashion. Nineteen segments are formed across the active detector area (Fig. 2). The pins are mounted in a Macor frame and are 2 mm apart with each wire segment exactly 50 mm long. The anode wire is maintained at +2150 V dc and is free of dust or imperfections which may result in electrical field amplification. Gas breakdown or arcing between the two electrodes significantly increases the overall noise of the system and, in some cases, may obscure photon-related events.

At the low energy boundary of the detector, the detection efficiency is influenced by the attenuation of the detector entrance window, dead zone, and Ni mesh. These variables all reduce the intensity of the incident x-ray photons prior to their arrival in the active detection area. In contrast, the main concern for high energy x-ray photons is the interaction with the gas atoms in the active detection area before the photons pass through the cathode plane undetected. The gas composition, gas pressure, and the anode-to-cathode distance become dominant factors.

To maximize the efficiency, the entrance window, dead zone, and Ni mesh should be as x ray transparent as possible—especially for the low energy range. The entrance window selected for this study balances the requirements for increased area, maximum x-ray transparency over the 4–6 keV energy range, and mechanical robustness for the large pressure differential expected during operation (approximately 1–2 atm). Similarly, the Ni mesh should allow maximum x-ray transmission by having sufficient open area and minimal thickness and also function as an efficient grounding plane with adequate mechanical strength. The dead zone is almost unavoidable due to the necessary presence of a clamping ring located over the beryllium window and Viton O-ring to permit gas sealing of the detector cham-

ber. The size of the dead zone for the detector developed in this study is 1 mm. Attenuation by the dead zone varies with gas pressure, and gas composition.

Additional factors required to optimize the detector efficiency include the gas composition and pressure. P10 yields optimum efficiency in the 4–6 keV energy range. The argon-methane density and therefore the attenuation within the active detection region are adjusted by altering the gas pressure. Low gas pressures are undesirable as too few atoms are present for sufficient interaction and subsequent avalanche formation. Conversely, reduced mean free paths of the ions caused by excessively high pressures can result in reduced avalanche charge formation and increase the probability of charge recombination. The detector employed in this study was evaluated over the pressure range of 1.00–1.50 atm (well within the high and low pressure limits). It was observed that the efficiency increased with increasing pressure over this range. A pressure of 1.25 atm was employed for the characterization tests to ensure that the maximum detector gas pressure was achieved without exceeding the safe limits for maintaining window integrity.

The anode-to-cathode distance and gas gain also affect the photon detection efficiency. The anode-to-cathode distance selected for the detector employed in this study is 5 mm. This is approximately 1.0–1.6 mm larger when compared to earlier work⁹ and increases the photon detection efficiency by 20.8%. Excessively large anode-to-cathode distances are undesirable because of increased charge recombination and degraded resolution, due to diffusion of the secondary ionization cloud as it moves towards the anode.^{11,12} The electric field strength and gas pressure affect the gas gain and therefore the avalanche size. For a given gas pressure, the anode voltage should maximize efficiency and minimize localized breakdown or arcing.

The gas composition, gas pressure, anode-to-cathode distance, and anode bias voltage also influence the resolution of the MWPC by changing the magnitude and distribution of the charge avalanche formed at the anode wire. Broadening mechanisms include extended ranges of high energy photoelectrons or Auger electrons in the active region of the detector after x-ray absorption, expansion of the secondary ionization cloud and centroid movement due to diffusion, fluctuation of the avalanche along the anode wire, and electronic noise from the signal processing electronics and data acquisition electronics.^{11–13} Some parameters that are optimized for maximum efficiency will adversely influence the resolution. Therefore a compromise between efficiency and resolution is sought.

III. SIGNAL GENERATION

In the past, resistive charge division techniques have been employed in photon counting applications where there is little requirement for accurate one or two dimensional representation. However, multidimensional encoding can be achieved by combining resistive charge division at the anode with other methods of encoding at the cathode. In the recent past, many MWPC designs combined resistive charge division with the popular delay line readout method incorporat-

ing microstrip designs on the cathode.¹⁴ Although this combination has proved very successful, the attachment of the resistors to each cathode segment is a tedious aspect of the design. Another successful cathode encoding option is the capacitive charge division technique. Due to its relatively simple construction and comparable performance to other encoding options, it is the selected design for the detector employed in this study. The detector operates in one-and-a-half dimension mode where the anode wires run parallel to the cathode segments. This arrangement is suitable for high-resolution x-ray spectroscopy applications where accurate encoding in one dimension (across the cathode board) and coarser resolution in the second dimension (bisecting the anode wires) are required.

Four signals are generated simultaneously for each photon detected—two from the anode wire and two from the cathode board. Charge pulses are detected at both ends of the wire as a consequence of the electron avalanche formed at the anode. Position encoding is determined by the principle of resistive charge division and is therefore dependent upon the position of the avalanche along the wire. The centroid of charge distributed over the various segments of the cathode board (below the avalanche site on the anode wire) provides high-resolution encoding via capacitive charge division.

IV. ELECTRONICS AND DATA ACQUISITION

The signal processing and data acquisition hardware schematic is shown in Fig. 3. The two primary objectives of the signal processing and data acquisition hardware are to ensure that the four detector signals originate from the same incident photon and to enable their digitization for subsequent data analysis. The incoming detector signals are preamplified (EG&G Ortec models 142AH and 142A), amplified, and shaped (Canberra model 2022) to form bipolar Gaussian pulses. These signals are split into two branches. The first set of pulses is directed into a quad single channel analyzer (EG&G Ortec model 850). Discriminators filter out low amplitude signals caused by noise and high amplitude signals resulting from cosmic radiation. The manually set values for low and high level discriminations range between 0.5–1.4 and 8.5–9.5 V, respectively. The four outputs from the quad single channel analyzer are fed into a universal coincidence module (EG&G Ortec model 418A) where all signals are compared to ensure that they are coincident within an input resolving time of 200 ns. If all four inputs originate from the same incoming photon, then a +5 V transistor-transistor logic (TTL) signal is generated and fed into a gate and delay generator (EG&G Ortec model 416A). The width of the +5 V TTL gate is 4 μ s and each gate is counted with a dual counter and timer module (EG&G Ortec model 994). All of the +5 V TTL pulses are converted to emitter coupled logic (ECL) pulses (amplitude of –750 mV and width of 4 μ s) and are employed to trigger the digitization process in the data acquisition hardware.

The second set of bipolar pulses is delayed (Canberra model 1457) by 4 μ s so that they reside within the ECL gate (generated from the first set of pulses). The delayed detector pulses are then directed into a 13 bit quad analog-to-digital

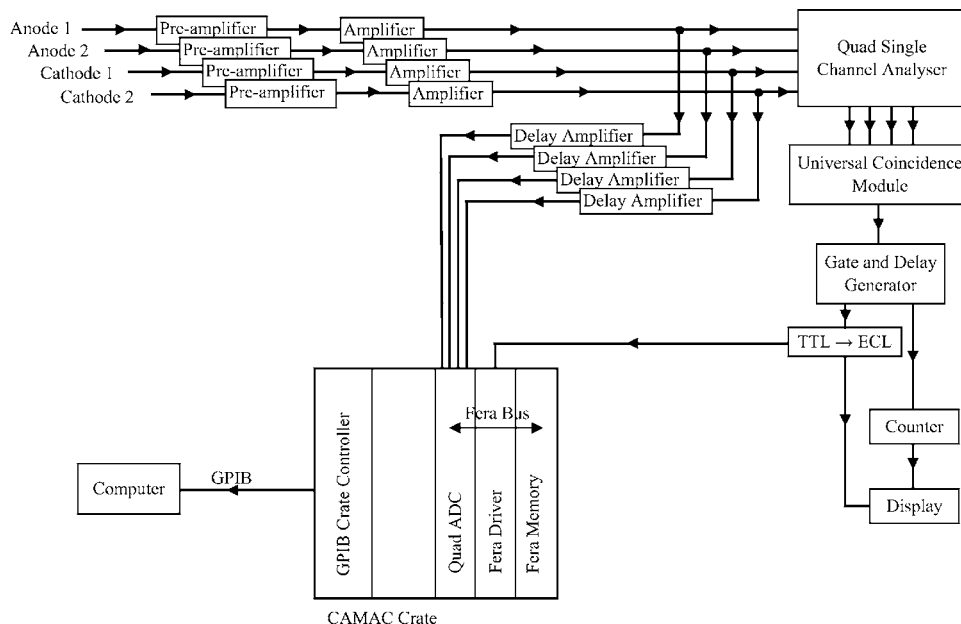


FIG. 3. Schematic of the data acquisition electronics used to identify coincident events and show data output.

converter (EG&G Ortec model AD413A) located in a CAMAC minicrate (Sparrow model 1000). The CAMAC bus is not employed in the transfer of the digitized data as it can be accomplished significantly faster on the fast encoder and readout (FERA) bus. The FERA driver module (LeCroy model 4301) is located in the CAMAC crate but uses the FERA bus to facilitate the data transfer within the CAMAC crate. The ECL gates trigger the FERA driver to enable the peak maximum within each gate to be digitized by the quad analog-to-digital converter. The digitized data are transferred on the FERA bus to the triple port fast memory module (LeCroy model 4302) where up to 16 kbytes of data can be stored before being transferred to the computer via the general purpose interface bus (GPIB) crate controller (Kinetic Systems Corporation model 3988-G3A/D3A). An Apple Macintosh G4 dual processor personal computer equipped with a National Instruments PCI-GPIB card and the software package K-max version 6.6.1f (Sparrow Incorporated) was employed to acquire, process, sort, and display the data.

V. TESTING PROCEDURE

Testing procedures were developed to assess the resolution and the linearity across the active detection region of the backgammon MWPC. Although the detector is capable of effective operation over a large energy range, the internal geometry and gas pressure were chosen for maximum photon detection efficiency for $V K\alpha_1$ (4.952 keV). This is the energy region of interest for our current high-resolution x-ray spectroscopy experiments.

A. Linearity

A MacScience rotating anode (model M18XH1, Japan) generated Cu $K\beta$ characteristic radiation that was monochromated to produce a Cu $K\beta$ line of width of 150–170 μm . Intensity measurements were taken in steps of 50 μm across

the face of the detector and each spectrum collected was fitted with a Gaussian function to determine the peak position.

B. Resolution

The resolution was measured using a Johann-type curved crystal spectrometer with the x rays generated from an external electron excited source. The x rays were diffracted by a curved Ge 220 crystal and focused approximately 1.35 m from the crystal (Fig. 4). The diffracted line width of $V K\alpha_1$ was measured with the backgammon detector and a CCD camera to assess the apparent broadening effects in the MWPC. Unlike flat crystal geometry where the resolution is usually defined by apertures, the resolution for the diffracted lines in Johann geometry is dependent only upon the source size, source-to-crystal distance, crystal-to-detector distance, crystal type, and curvature. The source size was roughly circular (2 mm in diameter) and was located 1050 mm from the crystal. No slits or apertures were used. The width of the monochromated $V K\alpha_1$ line was 401 μm and its height was approximately 38 mm (much larger than the diameter of the detection region) with no noticeable curvature.

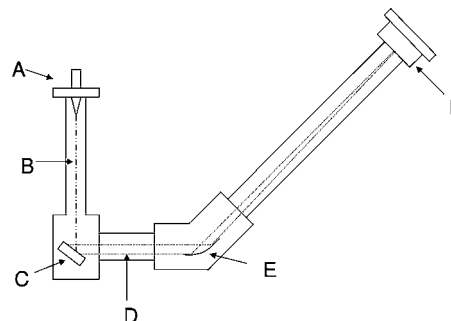


FIG. 4. Schematic of the Johann curved crystal x-ray focusing spectrometer: (A) electron gun, (B) electron beam path, (C) metallic foil, (D) characteristic x rays, (E) curved Ge 220 crystal, and (F) x-ray detector.

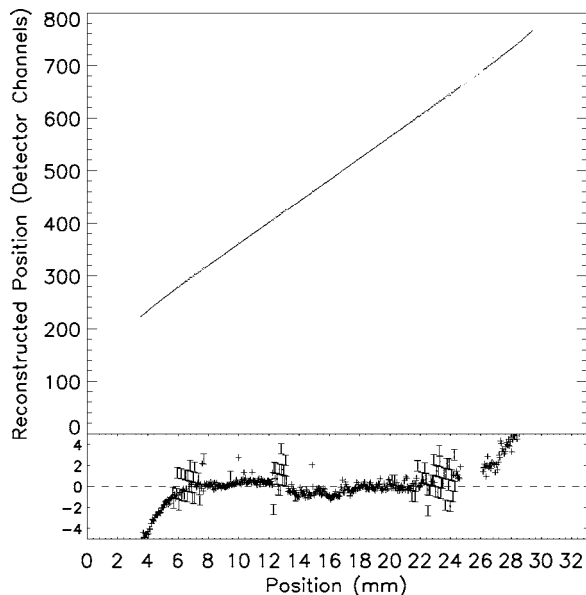


FIG. 5. A plot of detector response as a function of position across the face of the detector. The error bars (of one standard error) correspond to counting statistics at each position. The large error bars were measured for a shorter time but are included in the plot to illustrate the high overall consistency.

VI. RESULTS AND DISCUSSION

A. Linearity

From an initial qualitative assessment of the detector output as a function of position across the detector face (shown in Fig. 5), the detector appears highly linear, especially across the central open area of the detector face.

$$Y(\text{channels}) = (20.393\,89 \pm 0.000\,02)X(\text{mm}) + (156.4123 \pm 0.0003)(\text{channels}). \quad (1)$$

This long calibration procedure is required to obtain the statistical precision needed to prove the linearity as shown. A small selection of points in the residual subplot have larger error bars (one standard error shown only) corresponding to lower count statistics for these particular points. It is evident that the points are consistent with the smooth line and trend. Such deviations are expected from the statistics and suggest that the cathode board is uniform and the meandering wire is smooth.

Note that the remarkable linearity explains the accuracy attainable by this detector implementation, in two ways. The scale on the residual plot is $50\ \mu\text{m}$ per channel. Hence the smooth progression of data along the fitted line has a random or pointwise deviation from this line of a fraction of a channel, or perhaps $5\ \mu\text{m}$. Even this may be dominated by statistical considerations. Analysis of the residuals confirms the highly linear response with a standard deviation on the determined line, computed from the fitting function (1) of 9.8×10^{-7} or 0.0001% . Secondly, a collection of data covering a region shows the overall fitted uncertainty of the line, corresponding to an offset uncertainty of 3×10^{-4} channels or $0.015\ \mu\text{m}$.

Few other references provide equivalent quantification. Luther *et al.*⁹ also observed a good linear response in their detector, but their fractional linear range was significantly

20% less than our results and their linearity by this method of computation appears to be 0.002 or 0.2% compared to our value of 0.0001%.

The minor differential nonlinearity near the outer edges (the end 20%) is caused by the circular aperture of the detector window and is easily accounted for in modeling or removed by use of a square entrance window. The very edges of the “backgammon board” cannot be highly linear (to the level which we are discussing) and have never been so in past work. In part, this region depends upon the footprint size, the gas depth, and the aperture shape. We explicitly plotted this edge effect to show a feature or requirement of the detector type which is often not presented in papers. Most authors trim the edges, and indeed when collecting high-accuracy data we also do not collect from these extreme edges for this reason. Hence the proper definition of the differential nonlinearity is the nonlinearity of the operational active area, which, in fact, only excludes 2–3 mm from each end. The nonlinearity at the extremes is perhaps therefore a proof of the high linearity in the operationally active region.

The maximum fractional excursion from the line over the linear region (the operationally active region) is of order 0.002 or 0.2%, compared to the prior best value of 2%.⁹ Other references cite linearity errors $< 1\%$, without providing the corresponding plots of performance,¹⁵ or report figures of 1%.⁷

The differential nonlinearity is overestimated by the maximum fractional excursion, since it is likely dominated by the data collection process (i.e., outliers) rather than the intrinsic detector performance, so a local or regional differential nonlinearity is estimated from the residuals as approximately 0.025%. This is indeed based on the operational active region of the detector—that is the 20 mm width of the detector which is used for active measurements.

B. Efficiency

The x-ray photon detection efficiency is significantly energy dependent for all detectors. For the backgammon MWPC employed in this study, the largest influences on the efficiency are the entrance window composition and thickness, dead zone depth, Ni mesh thickness and open area, anode-to-cathode distance, gas composition, and gas pressure. A model calculating the total intensity loss of the x-ray photons entering and passing through each component of the detector describes the energy dependence (assuming all of the photon-gas interactions give rise to charge avalanche). The efficiency (ϵ) of the detector at each point on its surface is given by

$$\epsilon = [(e^{-(\mu/\rho)_w \rho_w t_w})(e^{-(\mu/\rho)_{dz} \rho_{dz} t_{dz}})(e^{-(\mu/\rho)_m \rho_m t_m}) \times (1 - e^{-(\mu/\rho)_{ar} \rho_{ar} t_{ar}})] \times 100\%, \quad (2)$$

where $(\mu/\rho)_w$ is the energy dependent mass attenuation coefficient for the beryllium entrance window, ρ_w is the density of the beryllium window, t_w is the thickness of the beryllium window, $(\mu/\rho)_{dz}$ is the energy dependent mass attenuation coefficient for the dead zone, ρ_{dz} is the density of the gas in the dead zone, t_{dz} is the thickness of the dead zone, $(\mu/\rho)_{ar}$ is the energy dependent mass attenuation coefficient for the ac-

TABLE I. The photon detection efficiency as a function of energy highlighting the losses from the Be window, dead zone, Ni mesh, and transmission through the detection volume.

Energy (keV)	Line	Be window (%T)	Dead zone (%T)	Ni mesh (%T)	Active volume attenuation (%)	Total eff. (%)
4.09	Sc $K\alpha_1$	71.1	75.7	85.9	71.6	38.6
4.51	Ti $K\alpha_1$	77.7	78.5	86.5	62.3	38.0
4.95	V $K\alpha_1$	82.7	81.1	89.5	53.0	35.5
5.41	Cr $K\alpha_1$	86.5	83.4	88.5	45.0	32.5
5.89	Mn $K\alpha_1$	89.4	85.5	89.7	37.9	29.0

tive detection region, ρ_{ar} is the density of the gas in the active detection region, and t_{ar} is the thickness of the active detection region.

From Eq. (2), the detector efficiency can be modeled for the detector employed in this study, and for other detectors of similar construction from other investigations. Based on the chosen parameters for window material, window thickness, dead zone thickness, gas pressure, gas composition, and anode-to-cathode distance, the results for the detector efficiency are shown in Table I over the energy range considered. The data highlight the loss mechanisms that reduce the photon detection efficiency. Low energy x-ray photons are less influenced by losses through the rear of the detector, but more sensitive to window, dead zone, and Ni mesh attenuation, whereas the opposite is true for the higher energy x-ray photons.

The data in Table I can identify key aspects of the detector to be optimized to improve the photon detection efficiency in different energy regimes. For example, improvements can be achieved for the lower energy range in the following ways: a thinner Be entrance window, a thinner Ni mesh with more open area, and the elimination of the dead zone. A more dramatic increase in photon detection efficiency is possible by increasing the attenuation of the P10 gas in the detection volume, e.g., by increasing the gas pressure. A gas pressure increase from 1.25 to 4.00 atm will increase the efficiency from 35.5% to 51.7% for V $K\alpha_1$. One should be careful of the mechanical robustness of the Be entrance window at such pressures.

C. Resolution

The detector resolution was extracted from the spectral profile of the V $K\alpha_1$ and V $K\alpha_2$ peaks (Fig. 6). The full width at half maximum (FWHM) measured on the CCD image of the V $K\alpha_1$ peak was $401 \pm 20 \mu\text{m}$, with broadening due to the natural width and source size. The corresponding image recorded on the backgammon-type MWPC yielded a FWHM for V $K\alpha_1$ of $520 \pm 30 \mu\text{m}$. Given that the actual resolution element of the CCD was $20 \mu\text{m}$, this determines the backgammon-type MWPC resolution to be $330 \pm 30 \mu\text{m}$ for these operating conditions. This value appears large compared to some key earlier studies ($80\text{--}200 \mu\text{m}$).⁸⁻¹⁰

Fischer *et al.*¹³ studied detector resolution as a function of gas composition and pressure. In general, MWPCs detecting x-ray photons with energies greater than 6 keV are usually filled with xenon gas compositions that are significantly

more efficient above 6 keV and are capable of superior resolution due to minimization of dispersion effects related to the photon-gas interaction mechanism and avalanche formation. References 8 and 9, which report lower resolution, use Xenon gas compositions and (therefore) test at the higher x-ray photon energy of Cu $K\alpha$. Factors such as x-ray energy, anode-to-cathode distance, gas composition, and gas pressure must be considered.

Deslattes¹⁶ raises one concern of position-sensitive proportional counters (PSPCs) in general due to their finite depth compared to CCDs, which affects resolution. Although finite depth clearly and obviously lowers the resolution of this detector type compared to a solid state (e.g., $20 \mu\text{m}$ pixel device), the attainable accuracy is often determined by the differential nonlinearity. A uniform cathode board and a smooth meander wire help to ensure that differential nonlinearities are particularly small, as we have shown. Deslattes also comments that the resolution is expected to be much poorer at low energies and low pressures, which confirms the earlier observations of Fischer *et al.*¹³

VII. SUMMARY

Future modifications are planned to improve both the efficiency and resolution of the backgammon-type MWPC. These include a thinner beryllium window, more x-ray trans-

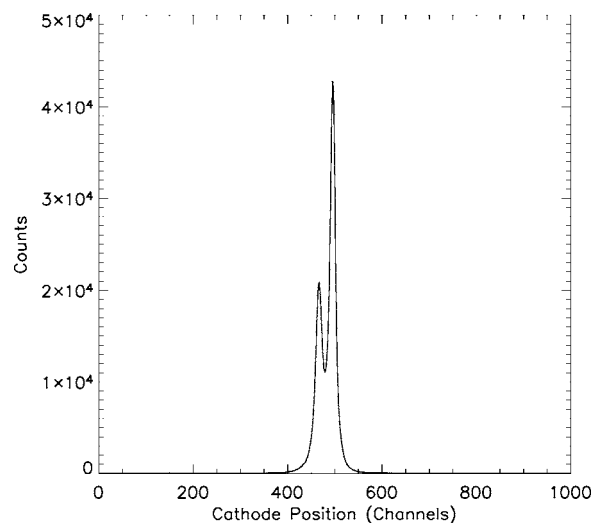


FIG. 6. The spectral profile from the backgammon-type MWPC showing clearly separated V $K\alpha_1$ (4.952 keV) and V $K\alpha_2$ peaks.

parent Ni mesh, thinner anode wire to improve the gas gain without increasing the bias voltage, and potentially higher gas pressure (from 1.25 herein to *circa* 4 atm in a different body design).

The current results, however, serve as an excellent benchmark for high precision low energy x-ray studies of all sorts and, in particular, for investigation in the 4–6 keV range. The differential nonlinearity by any measure is a strong result of this work, which has in part depended upon the detailed optimization discussed.

ACKNOWLEDGMENTS

The authors wish to thank David Paterson, George Christodoulou, Larry Hudson, and Albert Henins for their contributions to this work and general comments and support. The authors also wish to thank the Australian Research Council for funding this project.

- ¹G. Charpak, R. Bouchlier, T. Bressani, J. Favier, and C. Zupancic, Nucl. Instrum. Methods **62**, 235 (1968).
- ²G. Charpak, D. Rahm, and H. Steiner, Nucl. Instrum. Methods **80**, 13 (1970).
- ³C. T. Chantler, D. Paterson, L. T. Hudson, F. G. Serpa, J. D. Gillaspay, and E. Takacs, Phys. Rev. A **62**, 042501 (2000).
- ⁴J. D. Gillaspay, J. Phys. B **34**, R93 (2001).
- ⁵D. Paterson, C. T. Chantler, C. Q. Tran, L. T. Hudson, F. G. Serpa, and R. D. Deslattes, Phys. Scr., T **T73**, 400 (1997).
- ⁶C. T. Chantler and R. D. Deslattes, Rev. Sci. Instrum. **66**, 5123 (1995).
- ⁷R. Allemand and G. Thomas, Nucl. Instrum. Methods **137**, 141 (1976).
- ⁸B. P. Duval, J. Barth, R. D. Deslattes, A. Henins, and G. G. Luther, Nucl. Instrum. Methods Phys. Res. **222**, 274 (1984).
- ⁹G. G. Luther, P. L. Cowan, A. Henins, and S. Brennan, Nucl. Instrum. Methods Phys. Res. A **246**, 537 (1986).
- ¹⁰T. Mizogawa, M. Sato, and Y. Awaya, Nucl. Instrum. Methods Phys. Res. A **366**, 129 (1995).
- ¹¹G. C. Smith, J. Fischer, and V. Radeka, IEEE Trans. Nucl. Sci. **NS31**, 111 (1984).
- ¹²G. C. Smith, Nucl. Instrum. Methods Phys. Res. **222**, 230 (1984).
- ¹³J. Fischer, V. Radeka, and G. C. Smith, Nucl. Instrum. Methods Phys. Res. A **252**, 239 (1986).
- ¹⁴V. Radeka and R. A. Boie, Nucl. Instrum. Methods **178**, 543 (1980).
- ¹⁵P. L. Cowan, Nucl. Instrum. Methods Phys. Res. A **242**, 484 (1986).
- ¹⁶R. D. Deslattes, Rev. Sci. Instrum. **63**, 1128 (1992).